INORGANIC CHEMISTRY FRONTIERS

RESEARCH ARTICLE

View Article Online
View Journal | View Issue

Cite this: *Inorg. Chem. Front.*, 2025, **12**, 2506

Engineering tri-channel orthogonal luminescence in a single nanoparticle for information encryption†

Jianhao Zheng,[a,b] Pengye Du,[a,b] Ran An,*[a] Yuan Liang,[a] Yi Wei,[a] Shuyu Liu,[a,b] Pengpeng Lei*[a] and Hongjie Zhang *[a,b,c]

Received 12th December 2024,
Accepted 30th January 2025

DOI: 10.1039/d4qi03199g

rsc.li/frontiers-inorganic

Optical anti-counterfeiting technology based on the multicolor emission generated by the abundant energy levels of rare earth ions shows great potential in the face of increasing information security problems worldwide. However, it is not an easy task to achieve multi-channel orthogonal emissions in a single nanoparticle with a simple structure by a convenient method. In this work, we have successfully realized the tri-channel orthogonal emissions under three excitation wavelengths in $NaErF_4$@$NaYF_4$:Eu^{3+}@$NaBiF_4$:Yb^{3+},Tm^{3+} core@shell@shell nanoparticles. In our design, the interlayer $NaYF_4$:Eu^{3+} plays the role of "one arrow aiming at three eagles". First, it can enhance the upconversion luminescence intensity of $NaErF_4$. Next, it makes the emission color of Er^{3+} change from red to green by the energy transfer process between Er^{3+} and Eu^{3+}. Finally, it can produce red emission under 395 nm light excitation. This selective excitation strategy enables R-G-B tri-channel orthogonal emissions in a single nanoparticle by simply changing the excitation wavelength, which is very suitable for high level optical information encryption. This work provides a simple and effective method for the design of smart luminescent materials, showing great potential for multi-level anti-counterfeiting and information security.

10th anniversary statement

Congratulations on the 10th anniversary of *Inorganic Chemistry Frontiers*! Since its inception, a large number of high-quality articles have emerged, contributing to the prosperity of the subject of inorganic chemistry, which also includes more than ten works of our group. Over the past ten years, *Inorganic Chemistry Frontiers* has grown up together with inorganic chemists, leading the frontiers of inorganic chemistry exploration with excellent quality, rigorous attitude, and profound vision, and building a valuable platform for researchers to exchange and collide ideas. It is sincerely hoped that the journal will continue to maintain its advancement, innovate, and lead the future, making greater contributions to the progress of science and technology and the development of society.

1. Introduction

With the rapid development of social economy and technology, counterfeiting has become a global damaging problem with significant risks to national security, social development, and even human health.[1,2] Anti-counterfeiting technology safeguards authentic products from prying eyes and copying, and is important for protecting brands and valuable documents.[3–5] Innovation in anti-counterfeiting techniques that are difficult to replicate, easy to recognize and cost-effective is essential to combat this global challenge. Traditional anti-counterfeiting is often simple to crack, which highlights the need for advanced technology with high recognition and low cost. Currently, common anti-counterfeiting technologies mainly include laser holography, digital watermarking, fingerprint encryption, barcode, radio frequency identification, and optical anti-counterfeiting.[6–9] Among them, optical anti-counterfeiting with versatile properties can be altered by external stimuli such as the wavelength of excitation, pH, temperature, mechanical stimuli, and chemical environment, which can better satisfy the requirements of use and exhibit more complex performance.[10–13]

[a]*State Key Laboratory of Rare Earth Resource Utilization, Changchun Institute of Applied Chemistry, Chinese Academy of Sciences, Jilin, Changchun 130022, China. E-mail: anran@ciac.ac.cn, leipp@ciac.ac.cn, hongjie@ciac.ac.cn*
[b]*School of Applied Chemistry and Engineering, University of Science and Technology of China, Anhui, Hefei 230026, China*
[c]*Department of Chemistry, Tsinghua University, Beijing 100084, China*
† Electronic supplementary information (ESI) available. See DOI: https://doi.org/10.1039/d4qi03199g

Materials for optical anti-counterfeiting mainly include carbon dots, organic dye molecules, luminescent metal–organic frameworks, semiconductor quantum dots, metal halides, and rare earth luminescent materials.[14–17] According to their physical and chemical properties as well as structural characteristics, the luminescence performance should be optimized and regulated in terms of excitation wavelength, luminescence lifetime, and color to achieve integration and orthogonality in the same platform, so as to reach the purpose of single-level, double-level, and even multi-level anti-counterfeiting.[18–20] Focusing on luminescent colors, materials used for optical anti-counterfeiting need to have the ability to cover a wide spectral range as comprehensively as possible in order to realize multicolor emission with multiple excitation in one particle. The emission of rare earth luminescent materials covers the full spectrum of visible light from violet to red, and they have characteristic emission peaks in the ultraviolet (UV) and near-infrared regions (NIR), giving more tunability and selectivity for advanced anti-counterfeiting.[21,22] In addition, rare earth luminescent materials have narrow spectral bands of emission, high color purity, high resistance to photobleaching, stable physical and chemical properties, low toxicity, and long fluorescence lifetime, making them an excellent choice for optical anti-counterfeiting materials.[23,24] Rare earth ions can realize different types of emissions (*e.g.*, upconversion emission and downshifting emission) under NIR excitation and UV excitation, that is, exhibiting different luminescence properties under different excitation, further enhancing the versatility of rare earth luminescent materials for optical anti-counterfeiting.[25,26]

Variable excitation and emission arise from the complex energy level structure of rare earth ions. However, this is a double-edged sword. The richness of the energy level structure makes the possible energy transfer and cross-relaxation between ions more complex and diverse.[27–29] In contrast to optical anti-counterfeiting achieved using a co-mingling method that suffers from the problem of uneven mixing, the orthogonal luminescence achieved by constructing a core@shell structure on a single nanoparticle does not suffer from this problem. In practice, an inert intermediate layer without any activator is often introduced to achieve the effect of suppressing the undesired energy transfer between rare earth ions. Yet, it undoubtedly enlarges the number of shell layers of the particles, further increasing the complexity and difficulty of the preparation process, which is very unfavorable for the application of optical anti-counterfeiting.[30–32] It is one of the further problems that researchers need to address for developing new facile strategies for the preparation of multi-channel orthogonal rare earth nanoparticles or optimizing the existing means of construction.

In this work, we have constructed a kind of rare earth luminescent $NaErF_4$@$NaYF_4$:Eu^{3+}@$NaBiF_4$:Yb^{3+},Tm^{3+} nanoparticles consisting of only three-layer structures to achieve green (808 nm excitation), red (395 nm excitation), and blue (980 nm excitation) luminescence in a tri-channel orthogonal to each other, suitable for high-level optical anti-counterfeiting applications. The interlayer $NaYF_4$:Eu^{3+} plays the role of "one arrow aiming at three eagles". Firstly, it enhanced the upconversion luminescence (UCL) intensity of $NaErF_4$. Meanwhile, the Eu^{3+} regulated the core $NaErF_4$ to generate green light emission through the energy transfer process of Er^{3+} and Eu^{3+}. Moreover, it is also an activator of UV-excited red light emission. In the design of the outermost layer, we have compounded the $NaBiF_4$ host matrix of superior properties with $NaREF_4$ (RE stands for rare earth) for the first time. The low-toxicity green metal bismuth instead of expensive rare earth elements can greatly reduce the cost and be more relevant to practical applications. In conclusion, we have simplified the previous strategy of constructing routine rare earth nanoparticles with core@shell structures, realizing triple orthogonal emission in a three-layer structure, as well as broadening the way for applications in the fields of optical anti-counterfeiting and information encryption.

2. Experimental section

2.1 Materials

The raw materials, including erbium chloride hexahydrate ($ErCl_3{\cdot}6H_2O$, 99.9%), yttrium chloride hexahydrate ($YCl_3{\cdot}6H_2O$, 99.9%), europium chloride hexahydrate ($EuCl_3{\cdot}6H_2O$, 99.9%), ytterbium nitrate pentahydrate ($Yb(NO_3)_3{\cdot}5H_2O$, 99.9%), thulium nitrate ($Tm(NO_3)_3{\cdot}6H_2O$, 99.9%), analytical grade bismuth nitrate pentahydrate ($Bi(NO_3)_3{\cdot}5H_2O$, 99%), oleic acid (OA, AR), and 1-octadecene (ODE, 90%) were purchased from Aladdin Reagents (Shanghai, China). Sodium hydroxide (NaOH, 99.9%), sodium nitrate ($NaNO_3$, 99%), and ammonium fluoride (NH_4F, 98%) were purchased from Xilong (Guangdong, China). Ethylene glycol (EG) was obtained from Beijing Chemical Reagents (Beijing, China). All the above chemicals were used directly without further purification.

2.2 Synthesis of $NaErF_4$ core nanoparticles

The OA-capped $NaErF_4$ core nanoparticles were synthesized by a high-temperature solvothermal method. A typical procedure is as follows: $ErCl_3{\cdot}6H_2O$ (1 mmol) was added into a 100 mL three necked flask containing 6 mL OA and 15 mL ODE. The mixture was first heated to 150 °C to form a transparent solution and remove residual water, and then cooled down to room temperature. 50 mL of methanol solution containing NaOH (2.5 mmol) and NH_4F (4 mmol) was slowly dropped into the flask and stirred for 30 min. Then the solution was heated to 120 °C and maintained for 30 min to evaporate methanol. Subsequently, the solution was heated to 300 °C and maintained for 1 h under an argon atmosphere. After cooling down to room temperature, the resulting products were precipitated with ethanol and collected by centrifugation at 9000 rpm for 10 min. The precipitate was then purified with ethanol three times, and finally dispersed in 10 mL cyclohexane for further use.

2.2 Synthesis of $NaErF_4$@$NaYF_4$:*X*%Eu^{3+} core@shell nanoparticles

In a typical experiment, in a 100 mL three-necked flask containing 6 mL OA and 15 mL ODE given amounts of $YCl_3{\cdot}6H_2O$

(1–X mmol), $EuCl_3{\cdot}6H_2O$ (X mmol), and the $NaErF_4$ core (0.5 mmol) in cyclohexane were added. The mixture was heated to 150 °C to form a transparent solution, residual water and cyclohexane were removed and then cooled down to room temperature. 10 mL of methanol solution containing NaOH (2.5 mmol) and NH_4F (4 mmol) was slowly dropped into the flask and stirred for 30 min to ensure that all fluoride was completely consumed. Then the solution was heated to 120 °C for evaporating methanol completely from the reaction mixture. Subsequently, the solution was heated to 290 °C and maintained for 1 h under an argon atmosphere. After cooling down to room temperature, the resulting products were precipitated withethanol and collected by centrifugation at 9000 rpm for 10 min. The precipitate was then purified with ethanol three times, and finally dispersed in cyclohexane for further measurement and use.

2.3 Synthesis of $NaErF_4$@$NaYF_4$:*X*%Eu^{3+}@$NaBiF_4$:Yb^{3+},Tm^{3+} core@shell@shell nanoparticles

In a typical synthesis route, $Bi(NO_3)_3{\cdot}5H_2O$ (0.8 mmol), $Yb(NO_3)_3{\cdot}5H_2O$ (0.195 mmol), $Tm(NO_3)_3{\cdot}5H_2O$ (0.005 mmol), and $NaNO_3$ (2 mmol) were dissolved in 5 mL EG solution. Then the core@shell nanoparticles dispersed in cyclohexane were centrifuged at 9000 rpm with ethanol, immediately 5 ml EG was added to the centrifugation product in a wet state and the nanoparticles were ultrasonically dispersed until forming a homogeneous solution. Then, these two solutions were mixed with continuous stirring for 30 min. A certain quantity (24 mmol) of NH_4F in 25 mL of EG was added to the above mixtures under vigorous stirring for 30 min. After stirring uniformly, the mixed solution was transferred to a Teflon-lined autoclave (50 mL) and the reaction conditions of the oven were set to 150 °C for 8 h. After the reaction, the autoclave was naturally cooled and taken out. Next, the samples were washed four times with anhydrous ethanol and collected through centrifugation. Finally, the products were dried at room temperature for further measurement.

2.4 Characterization

Low-/high-resolution transmission electron microscopy (TEM) were carried out on a FEI Tecnai G2S-Twin instrument with a field-emission gun operating at 200 kV. X-ray photoelectron spectroscopy (XPS) measurements were performed using a Thermo ESCALAB 250XI spectrometer. The fluorescence spectra were recorded using a fluorescence spectrofluorometer (Edinburgh Instruments, FLSP-920) equipped with an NIR continuous wave laser with emission at 980 nm or 808 nm. The morphology and composition of the crystals were examined using a field-emission scanning electron microscope (FE-SEM, S-4800, Hitachi) equipped with an energy-dispersive X-ray spectrometer (EDS). Powder X-ray diffraction (PXRD) patterns of the crystals were obtained using a D8 Focus diffractometer (Bruker) with Cu Kα radiation (λ = 1.5418 Å) with the operation voltage and current remaining at 40 kV and 40 mA. All measurements were performed at room temperature.

3. Results and discussion

3.1 Morphology, structure, and composition

The whole tri-channel orthogonal emission mechanisms and the optical anti-counterfeiting applications of the $NaErF_4$@$NaYF_4$:Eu^{3+}@$NaBiF_4$:Yb^{3+},Tm^{3+} nanoparticles can been seen in Fig. 1. We first synthesized core@shell nanoparticles $NaErF_4$@$NaYF_4$:Eu^{3+} by a two-step high-temperature solvothermal method,[33] and then synthesized the core@shell@shell nanoparticles $NaErF_4$@$NaYF_4$:Eu^{3+}@$NaBiF_4$:Yb^{3+}, Tm^{3+} by a hydrothermal approach.[34] Typically, pure $NaErF_4$ core nanocrystals were first prepared and used as seeds for subsequent epitaxial growth of a $NaYF_4$:Eu^{3+} shell, and finally hydrothermally coated with a $NaBiF_4$:Yb^{3+},Tm^{3+} shell. As can be seen from representative transmission electron microscopy (TEM) images (Fig. 2a–c), the obtained $NaErF_4$ core nanoparticles, the $NaErF_4$@$NaYF_4$:Eu^{3+} core@shell nanoparticles,

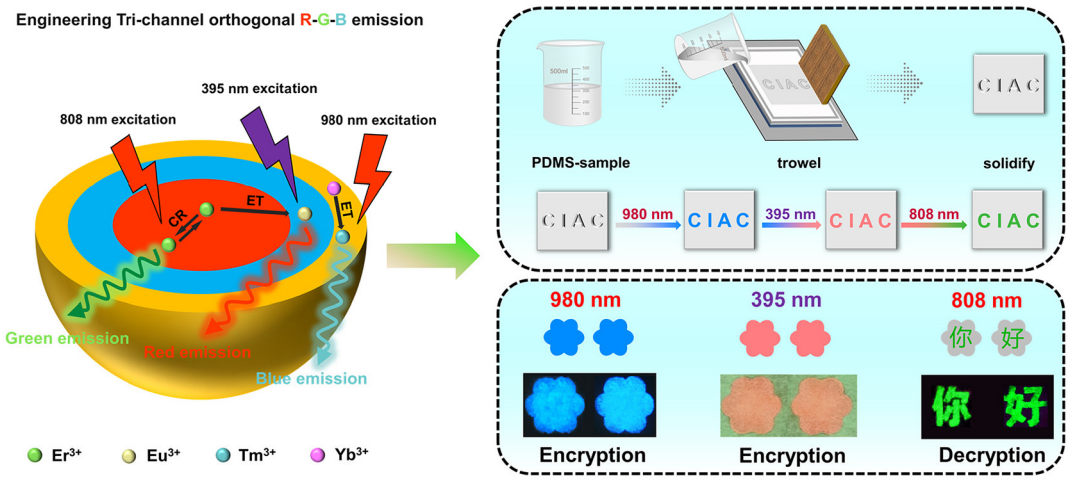

Fig. 1 Schematic illustration of engineering tri-channel orthogonal luminescence and the optical anti-counterfeiting applications of the $NaErF_4$@$NaYF_4$:Eu^{3+}@$NaBiF_4$:Yb^{3+},Tm^{3+} nanoparticles.

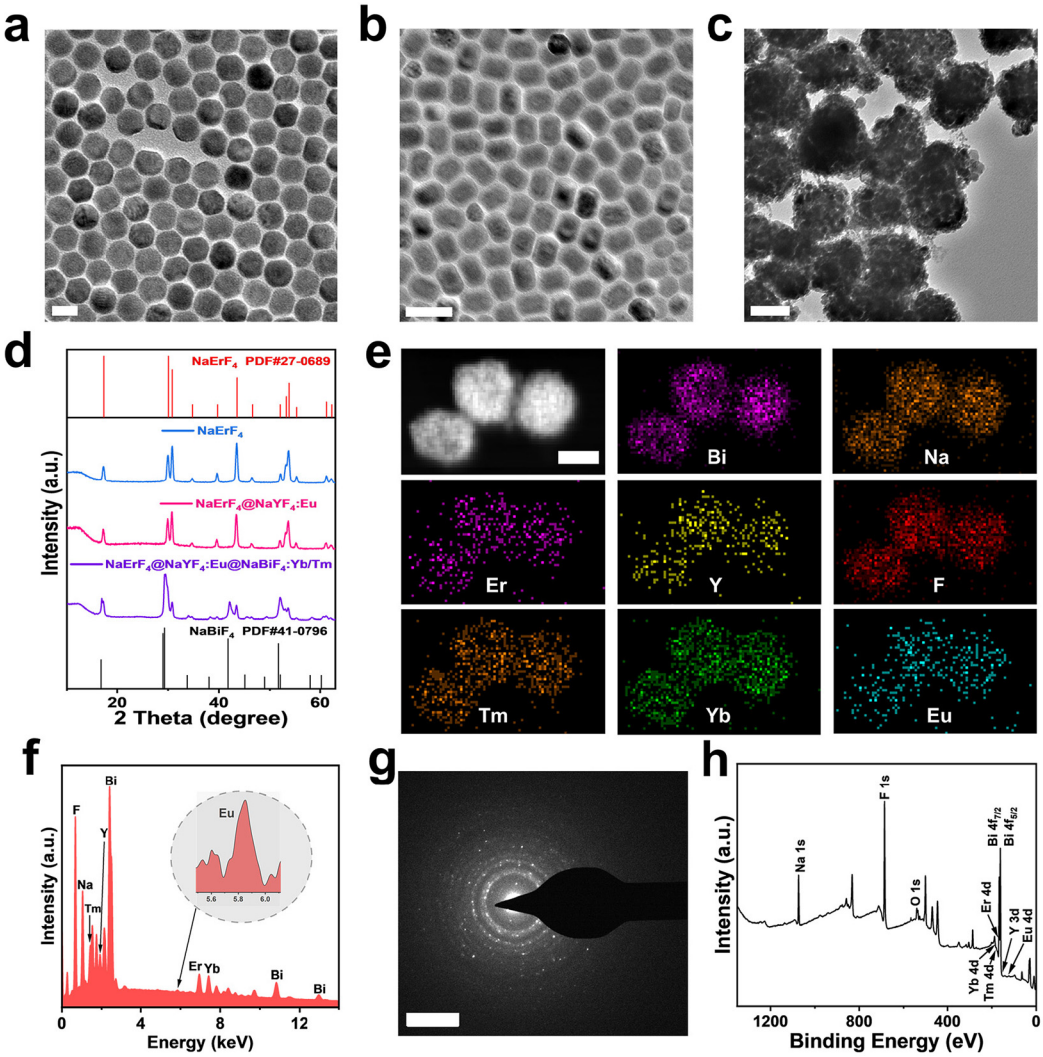

Fig. 2 TEM images of (a) $NaErF_4$, (b) $NaErF_4$@$NaYF_4$:Eu^{3+}, and (c) $NaErF_4$@$NaYF_4$:Eu^{3+}@$NaBiF_4$:Yb^{3+},Tm^{3+} (scale bar: 20 nm, 50 nm, and 100 nm, respectively). (d) XRD patterns of $NaErF_4$, $NaErF_4$@$NaYF_4$:Eu^{3+}, and $NaErF_4$@$NaYF_4$:Eu^{3+}@$NaBiF_4$:Yb^{3+},Tm^{3+} nanoparticles. (e) High-angle annular dark-field scanning transmission electron microscopy image and element mappings of Bi, Na, Er, Y, F, Tm, Yb, and Eu (scale bar: 100 nm). (f) EDS spectra of the $NaErF_4$@$NaYF_4$:Eu^{3+}@$NaBiF_4$:Yb^{3+},Tm^{3+}. (g) Selected area electron diffraction (SAED) patterns of the $NaErF_4$@$NaYF_4$:Eu^{3+}@$NaBiF_4$:Yb^{3+},Tm^{3+} nanoparticles (scale bar: 51 nm^{-1}). (h) The XPS survey spectrum of the $NaErF_4$@$NaYF_4$:Eu^{3+}@$NaBiF_4$:Yb^{3+},Tm^{3+} nanoparticles.

and $NaErF_4$@$NaYF_4$:Eu^{3+}@$NaBiF_4$:Yb^{3+},Tm^{3+} core@shell@shell nanoparticles have a homogeneous morphology and monodisperse particle-size distributions, with the average sizes of 20.8 nm, 36.4 nm in length and 27.1 nm in width, and 175.7 nm, respectively (Fig. S1†). It is evident that the high-resolution TEM images in Fig. S2† exhibit distinct lattice fringes and the distances between these adjacent lattices are demonstrated to be around 0.51 nm, 0.52 nm, and 0.308 nm which are associated with the (100) plane of hexagonal $NaErF_4$, (100) plane of hexagonal $NaYF_4$, and (110) plane of hexagonal $NaBiF_4$, respectively.[19,35] The X-ray diffraction (XRD) patterns show that these three nanoparticles, $NaErF_4$, $NaErF_4$@$NaYF_4$:Eu^{3+}, and $NaErF_4$@$NaYF_4$:Eu^{3+}@$NaBiF_4$:Yb^{3+},Tm^{3+}, are in the pure phase, which in agreement with the arrangement of the standard $NaErF_4$ and $NaBiF_4$ phases (Fig. 2d). Then, corresponding energy dispersive X-ray spectroscopy (EDS) mapping of several randomly selected $NaErF_4$@$NaYF_4$:Eu^{3+}@$NaBiF_4$:Yb^{3+},Tm^{3+} nanoparticles (Fig. 2e and f) verified the distribution of Er, Y, Eu, Yb, Tm, Bi, Na, and F, confirming that the core@shell@shell nanostructure was successfully constructed. More importantly, it is clearly seen that Bi is distribute in the shell layer, while Y is present in the core region. Meanwhile, as shown in Fig. 2g, selected area electron diffraction (SAED) patterns of the $NaErF_4$@$NaYF_4$:Eu^{3+}@$NaBiF_4$:Yb^{3+},Tm^{3+} nanoparticles represent a high crystallinity of the synthesized materials. Furthermore, X-ray photoelectron spectroscopy (XPS) was performed to determine the electronic states and chemical properties of the prepared samples. The survey spectrum of the $NaErF_4$@$NaYF_4$:Eu^{3+}@$NaBiF_4$:Yb^{3+},Tm^{3+} nanoparticles also showed in Fig. 2h confirms the presence of Er, Y,

Eu, Bi, Tm, Yb, Na, and F elements. The binding energy peaks located at 165.6 and 160.2 eV are attributed to Bi $4f_{5/2}$ and Bi $4f_{7/2}$ of Bi^{3+}, while the peaks of 157.1 and 162.0 eV are affiliated to Y $3d_{5/2}$ and Y $3d_{3/2}$ of Y^{3+} (Fig. S3a†). The peak appearing at 1071.8 eV belongs to the binding energy of Na^+ 1s (Fig. S3b†). The three peaks located at 169.8 eV, 177.9 eV, and 186.1 eV are attributed to the binding energies of Er 4d, Tm 4d, and Yb 4d, respectively (Fig. S3c†). The peaks centered at 684.6 eV and 137.1 eV belong to the binding energy of F 1s and Eu 4d (Fig. S3d and S3e†). These pieces of evidence substantiated the successful synthesis of $NaErF_4$@$NaYF_4$:Eu^{3+}@$NaBiF_4$:Yb^{3+},Tm^{3+} nanoparticles, which ensured the realization of efficient tri-channel orthogonal emissions.

3.2 Tri-channel orthogonal luminescent $NaErF_4$@$NaYF_4$:Eu^{3+}@$NaBiF_4$:Yb^{3+},Tm^{3+} core@shell@shell nanoparticles

In order to investigate the fluorescence properties of nanoparticles, core@shell nanostructures of $NaErF_4$@$NaYF_4$:*X*% Eu^{3+} (*X* = 0, 5, 10, and 15) with four different Eu^{3+} doping amounts were first designed and prepared. Then, the corresponding XRD and TEM images clearly showed that the synthesized nanoparticles essentially matched well with the pristine $NaErF_4$ phase, which demonstrated that the nanoparticles are of high phase purity and uniform in shape and size (Fig. S4 and S5†). The excitation and emission spectra of these synthesized core@shell samples were studied. By comparing the emission spectra of Er^{3+} (λ_{ex} = 808 nm) in the core@shell nanoparticles, it was found that when the interlayer is doped with Eu^{3+}, it can lead to a significant enhancement of the ratio of green emission ($^2H_{11/2}$, $^4S_{3/2} \rightarrow {}^4I_{15/2}$) intensity and the red emission ($^4F_{9/2} \rightarrow {}^4I_{15/2}$) intensity in Fig. 3a and S6,† which indicates the occurrence of the Er and Eu energy transfer process.[36–38] As shown in Fig. 3b, compared with the undoped samples, for Eu^{3+} doped samples, the luminescence color changes from red to green under an 808 nm laser, and the corresponding CIE color coordinates remain basically unchanged with the increase of the doping concentration of Eu^{3+}. In addition, we have also measured the time-resolved photoluminescence (TRPL) decay curves of the $NaErF_4$@$NaYF_4$:*X*% Eu^{3+} (*X* = 0, 5, 10, and 15) samples, and then systematically analyzed the luminescence dynamics. As shown in Fig. 3c, the TRPL decay curves of the crystals with different amounts of Eu^{3+} can be well fitted by using single exponential decay curves. As the Eu^{3+} doping amount increases, the corresponding lifetimes of samples at 540 nm with the $^4S_{3/2} \rightarrow {}^4I_{15/2}$ transition of Er^{3+} are 0.251 ms, 0.209 ms, 0.188 ms, and 0.156 ms, respectively (Fig. S7†). The decreasing lifetimes are mainly attributed to the gradual intensification of the Er^{3+} and Eu^{3+} energy transfer process, which causes the decreasing population of the $^4S_{3/2}$ energy level of Er^{3+}.[28,39,40] Furthermore, we investigated the variation of the red emission intensity at different doping amounts of Eu^{3+}.

The excitation spectrum in Fig. S8† shows that there is a strong absorption peak at 395 nm, which indicates that the best emission intensity can be obtained after excitation of the sample at this wavelength; so we chose to use the UV excitation at 395 nm. The photoluminescence spectra were further tested under different doping amounts of Eu^{3+}. From the pseudo-

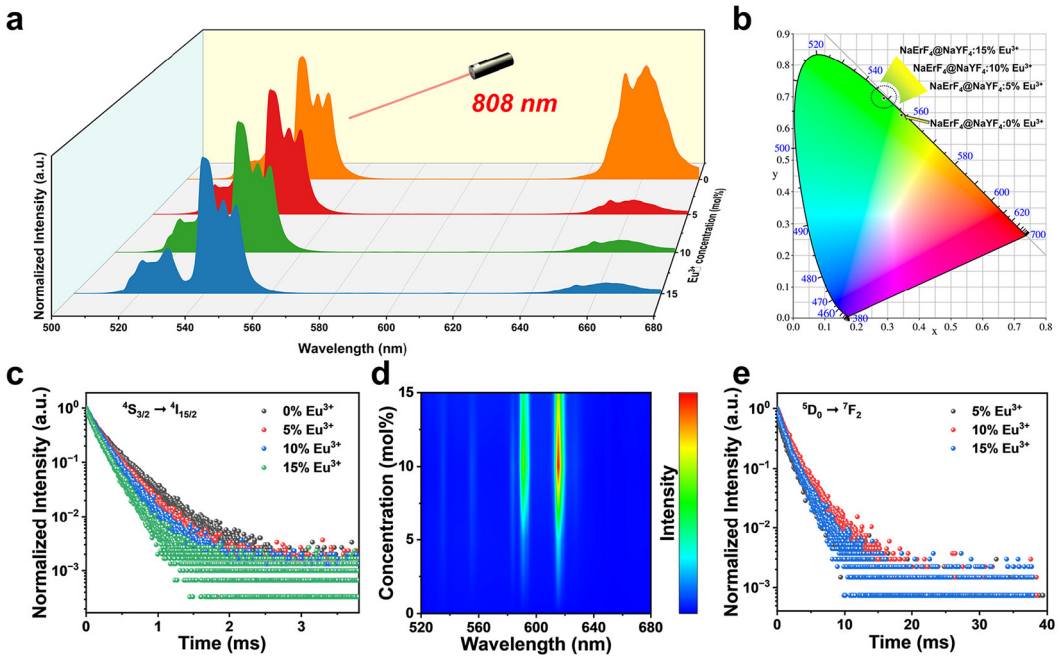

Fig. 3 (a) UC spectroscopy of $NaErF_4$@$NaYF_4$:*X*% Eu^{3+} (*X* = 0, 5, 10, and 15) nanoparticles under an 808 nm laser (laser power density: 7.5 W cm^{-2}) and (b) its corresponding CIE coordinates. (c) PL decay curves (probed at 539 nm) for the $NaErF_4$@$NaYF_4$:*X*% Eu^{3+} (*X* = 0–15) nanoparticles under the 808 nm laser. (d) The pseudo-color spectrum of the $NaErF_4$@$NaYF_4$:*X*% Eu^{3+} (*X* = 0–15) nanoparticles under 395 nm light. (e) PL decay curves (probed at 615 nm) for the $NaErF_4$@$NaYF_4$:*X*% Eu^{3+} (*X* = 5, 10, and 15) nanoparticles under 395 nm light.

color spectra of the $NaErF_4$@$NaYF_4$:X% Eu^{3+} (X = 0, 5, 10, and 15) nanoparticles (Fig. 3d), it can be clearly seen that, with the increase of Eu^{3+} doping concentration, the intensity of the emission peak at 615 nm, which belongs to $^5D_0 \rightarrow {}^7F_2$ transition of Eu^{3+}, firstly increases and then decreases, and the highest emission intensity is found at a doping concentration of 10%. Furthermore, the corresponding TRPL decay curves show that the lifetime variations are also consistent with the emission intensity trend, with the longest lifetime at a Eu^{3+} doping concentration of 10% (Fig. 3e and S9†). Combining the photoluminescence performance of the $NaErF_4$@$NaYF_4$:X% Eu^{3+} (X = 0, 5, 10, and 15) nanoparticles under a 808 nm laser and 395 nm light, it was determined that the best orthogonal luminescence was achieved in the $NaErF_4$@$NaYF_4$:10% Eu^{3+} nanoparticles.

Encouraged by the excellent orthogonal luminescence performance of $NaErF_4$@$NaYF_4$:10% Eu^{3+} nanoparticles, we further grew a $NaBiF_4$:Yb^{3+},Tm^{3+} shell layer, which was coated outside the $NaErF_4$@$NaYF_4$:10% Eu^{3+} core@shell nanoparticles to achieve the triple-channnel orthogonal luminescence. This is the first work on the $NaREF_4$ nanoparticles coated with a $NaBiF_4$ matrix. Fig. 4a shows the energy transfer path of the core@shell@shell $NaErF_4$@$NaYF_4$:10% Eu^{3+}@$NaBiF_4$:Yb^{3+},Tm^{3+} nanoparticles, which produce distinctly different luminescence colors under three different excitation light. As shown in Fig. 4b–d, the samples can generate blue light ($^1G_4 \rightarrow {}^3H_6$, $^1D_2 \rightarrow {}^3F_4$), red light ($^5D_0 \rightarrow {}^7F_1$, $^5D_0 \rightarrow {}^7F_2$), and green luminescence ($^2H_{11/2} \rightarrow {}^4I_{15/2}$, $^4S_{3/2} \rightarrow {}^4I_{15/2}$) under the excitation of 980, 395, and 808 nm lasers, respectively, and the lifetime of the 475 nm emission of Tm^{3+} is 2.06 ms (Fig. S10†). All these phenomena confirm that the nanoparticles have very good tri-channel orthogonal luminescence properties, which is dependent on the wavelength of the excitation light. In order to further verify the number of photons involved in the fluorescence of $NaErF_4$@$NaYF_4$:10% Eu^{3+}@$NaBiF_4$:Yb^{3+},Tm^{3+} nanoparticles under 808 and 980 nm lasers, respectively, UCL spectra with different excitation laser power densities were investigated. The fluorescence intensity

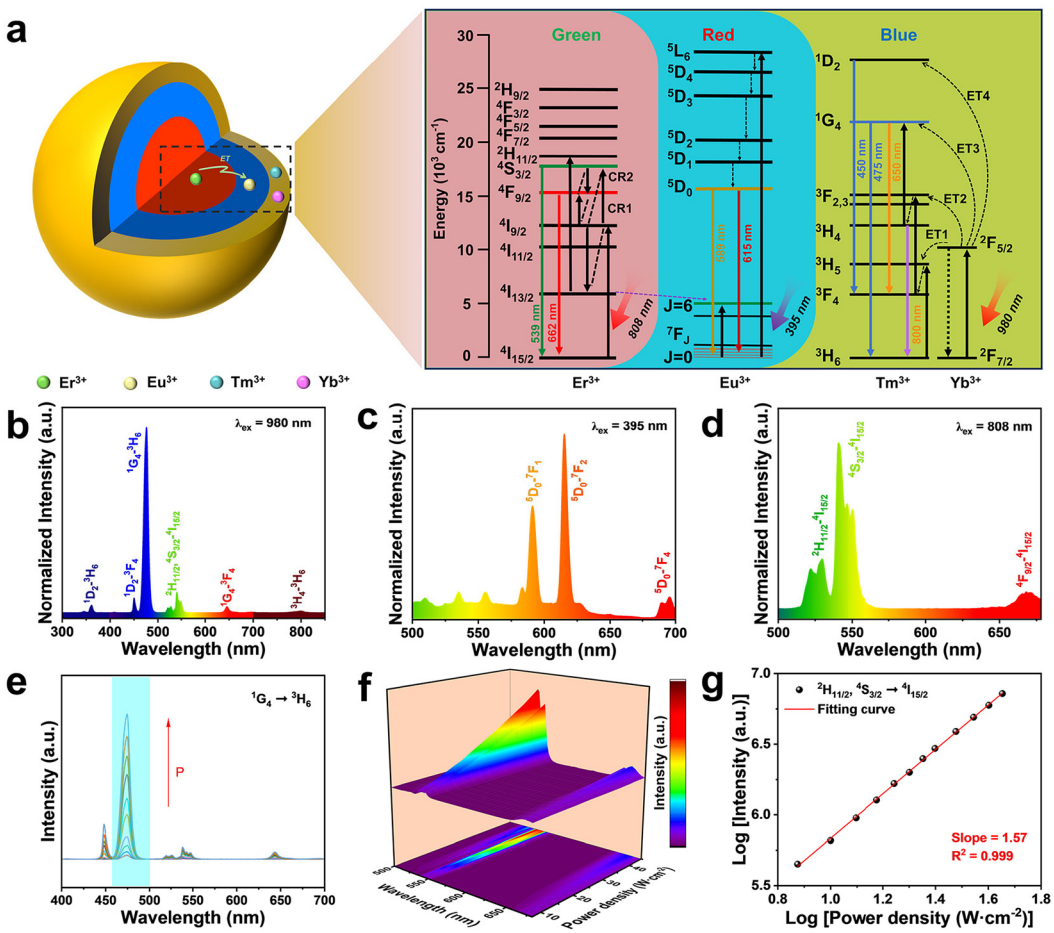

Fig. 4 (a) Schematic of the red, green, and blue tri-color emissions under 808, 395, and 980 nm excitation, respectively. The fluorescence spectroscopy of the $NaErF_4$@$NaYF_4$:10% Eu^{3+}@$NaBiF_4$:Yb^{3+},Tm^{3+} nanoparticles under (b) a 980 nm laser (laser power density: 7.5 W cm^{-2}), (c) 395 nm light, and (d) a 808 nm laser (laser power density: 7.5 W cm^{-2}). (e) Power-dependent UCL spectrum of the $NaErF_4$@$NaYF_4$:10% Eu^{3+}@$NaBiF_4$:Yb^{3+}, Tm^{3+} nanoparticles with excitation laser power densities between 3.275 and 18.6 W cm^{-2} under the 980 nm laser. (f) UCL spectra of $NaErF_4$@$NaYF_4$:10% Eu^{3+}@$NaBiF_4$:Yb^{3+},Tm^{3+} with excitation laser power densities between 7.5 and 45 W cm^{-2} under the 808 nm laser. (g) Pump power dependence of the $^2H_{11/2}$, $^4S_{3/2} \rightarrow {}^4I_{15/2}$ transition under 808 nm excitation.

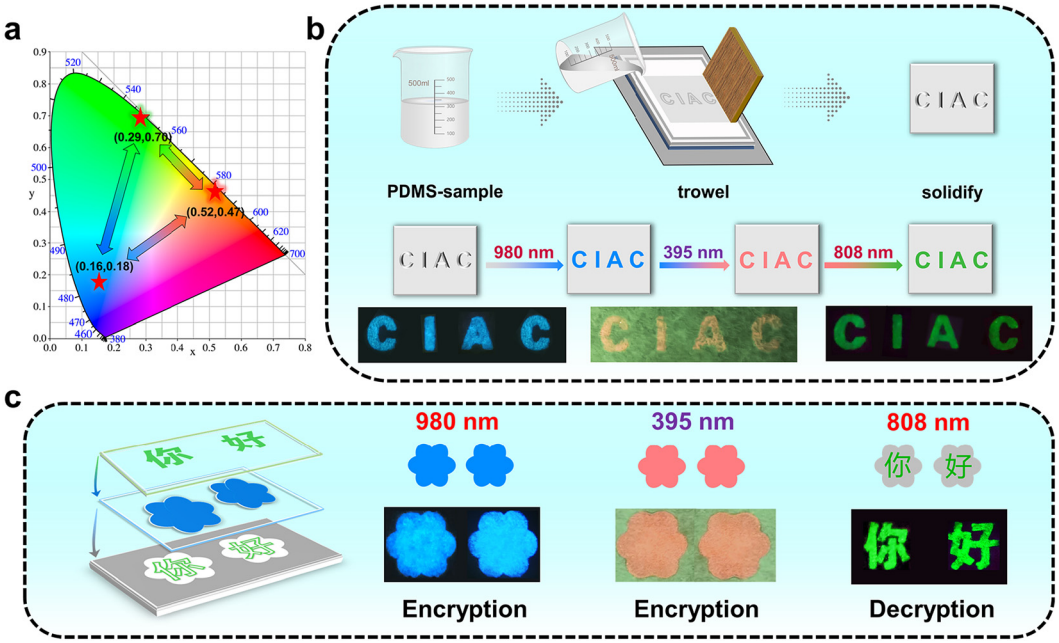

Fig. 5 Color-switchable output for information encryption. (a) CIE chromatic coordinates for the tri-color emission profiles from the $NaErF_4$@$NaYF_4$:Eu^{3+}@$NaBiF_4$:Yb^{3+},Tm^{3+} nanoparticles and (b) the corresponding "CIAC" patterns with tri-channel orthogonal emissions displayed. (c) Photographs of films with a tri-channel orthogonal anti-counterfeiting schematic diagram under 980 (left), 395 (middle), and 808 nm (right) laser excitation, respectively.

(I) and power density (P) show a relationship of $I \propto P^n$, where n is the number of photons absorbed per emission.[41] As shown in Fig. 4e, with 980 nm excitation, all the emissions gradually increase with increasing excitation power density, especially the $^1G_4 \rightarrow {}^3H_6$ transition. Similarly, for 808 nm excitation, a strong power dependence of the $^2H_{11/2} \rightarrow {}^4I_{15/2}$ and $^4S_{3/2} \rightarrow {}^4I_{15/2}$ transitions belonging to Er^{3+} is evident in Fig. 4f. Fig. 4g and S11† show the LogI *versus* LogP plots of this relationship, and thus the n-value was quantified by the slope of the linear fitting curves. Under the excitation of a 980 nm laser, the n-values of the $^1G_4 \rightarrow {}^3H_6$ transition is 2.1, indicating that the three-photon absorption process predominantly involves Tm^{3+}. As for Er^{3+} UC emissions under the 808 nm laser, the related n-value is 1.57, which indicates that the two-photon absorption process leads to the visible UC emissions. The slopes are much less than standard 3 and 2 for three and two photons and may be ascribed to the saturation effect reducing the power dependence of emissions.[42] The determination of the pump photon number further confirms the energy transfer process described above.

3.3 Applications

Based on the CIE color coordinates shown in Fig. 5a and the corresponding tri-color emissions of the samples (Fig. 5b), the excellent tri-channel orthogonal emission capability is confirmed. Based on this, we further explored its feasibility in anti-counterfeiting applications. As a proof-of-concept experiment, two types of the $NaErF_4$@$NaYF_4$:10% Eu^{3+} and the $NaErF_4$@$NaYF_4$:10% Eu^{3+}@$NaBiF_4$:Yb^{3+},Tm^{3+} nanoparticles were used, and these fluorescent nanoparticles were dispersed in PDMS solution to fabricate security inks. The 2D-encoded patterns including Arabic numerals and characters were trowelled on A4 paper by the obtained inks. Firstly, we show its double-color anti-counterfeiting capacity under a NIR laser. Apparently, the 2D-encoded double-color patterns showed the wrong information "**8888**" under an 808 nm NIR laser, and only under the excitation of a 980 nm laser, their characteristic digits "**2024**" could be easily recognized (Fig. S12†). These results demonstrate the remarkable double-color encryption capability of our materials under the NIR laser, providing a high level of security for anti-counterfeiting applications. To further demonstrate the performance of the synthesized nanoparticles for three-channel orthogonal anti-counterfeiting, the Chinese character "**你好**" was printed in the flower pattern, as shown in Fig. 5c. Under the irradiation of 980 nm laser or 395 nm UV light, only the wrong 2D pattern "**flower**" can be observed by the naked eye, while only under the excitation of 808 nm NIR laser, the coded information Chinese character "**你 好**" can be realistically revealed. In conclusion, the designed nanoparticles with color-tunable tri-channel emissions under different excitation wavelengths are promising in the field of advanced anti-counterfeiting.

4. Conclusions

In summary, we have successfully achieved red, green, and blue light from a single $NaErF_4$@$NaYF_4$:10% Eu^{3+}@$NaBiF_4$:Yb^{3+},Tm^{3+} nanoparticle under three kinds of excitation wavelengths by constructing a core@shell@shell structure. The

interlayer $NaYF_4$:Eu^{3+} plays an important role in this nanoparticle. Firstly, the $NaYF_4$:Eu^{3+} middle layer can enhance the UCL intensity of the inner core $NaErF_4$ by reducing the surface quenching. Secondly, the introduction of Eu^{3+} facilitates the UC emission color of the Er^{3+} activator to be tuned from red to green by the energy transfer process between Er^{3+} and Eu^{3+}. Finally, Eu^{3+} itself can be excited by UV light at 395 nm to emit red light. More importantly, we have successfully realized the coating of a $NaBiF_4$ matrix shell layer on the outside of the $NaREF_4$ nanoparticles for the first time. These results provide a conceptual model for the realization of versatile TIR-channel orthogonal emission, which shows great opportunities in a variety of advanced security designs and full-color displays. It is crucial for the development of the next generation of smart luminescent materials for diverse cutting-edge applications.

Author contributions

Jianhao Zheng: investigation, methodology, data curation, and writing – original draft. Pengye Du: data curation and investigation. Ran An: conceptualization and writing – review and editing. Yuan Liang: data curation and formal analysis. Yi Wei: methodology. Shuyu Liu: formal analysis. Pengpeng Lei: writing – review and editing and funding acquisition. Hongjie Zhang: conceptualization, writing – review and editing, and funding acquisition.

Data availability

The data that support the findings of this study are available from the corresponding author upon reasonable request.

Conflicts of interest

There are no conflicts to declare.

Acknowledgements

This work was supported financially by the National Natural Science Foundation of China (52371254) and the Program of Science and Technology Development Plan of Jilin Province of China (YDZJ202302CXJD065).

References

1 Z. Ma, X. Ji, S. Lin, X. Chen, D. Wu, X. Li, Y. Zhang, C. Shan, Z. Shi and X. Fang, Recent advances and opportunities of eco-friendly ternary copper halides: A new superstar in optoelectronic applications, *Adv. Mater.*, 2023, **35**, 2300731.

2 S. Jia, B. Yang, J. Du, Y. Xie, L. Yu, Y. Zhang, T. Tao, W. Tang and J. Gong, Uncovering the recent progress of cnc-derived chirality nanomaterials: Structure and functions, *Small*, 2024, **20**, 2401664.

3 Z. Xu, P. Li, H. Sun and Q. Zhang, Multicolor real-time and differentiation displays in $NaNbO_3$-based photochromics for advanced anti-counterfeiting applications, *Ceram. Int*, 2024, **50**, 27661–27670.

4 R. An, J. Hao, S. Song, H. Zhang, J. Feng, X. Wang and H. Sun, Multi-responsive 0d organic–inorganic hybrid cuprous bromides constructed via ultra-facile approaches for multimodal luminescent anti-counterfeiting, *Adv. Opt. Mater.*, 2023, **11**, 2202596.

5 Z. Zhang, H. Li, R. Pang, D. Li, L. Jiang, S. Zhang and H. Zhang, Manipulating photon absorption and trap energy supply for multimode dynamic anti-counterfeiting, *Inorg. Chem. Front.*, 2024, **11**, 4401–4414.

6 Y. Shi, S. Zhao, Y. Zhou and Z. Zang, Variable halide perovskites: Diversification of anti-counterfeiting applications, *Mater. Chem. Front.*, 2023, **7**, 6085–6106.

7 Z. Chen, H. Zhu, J. Qian, Z. Li, X. Hu, Y. Guo, Y. Fu, H. Zhu, W. Nai, Z. Yang, D. Li and L. Zhou, Rare earth ion doped luminescent materials: A review of up/down conversion luminescent mechanism, synthesis, and anti-counterfeiting application, *Photonics*, 2023, **10**, 1014.

8 B.-M. Liu, Y. Lin, Y. Liu, B. Lou, C.-G. Ma, H. Zhang and J. Wang, Excitation-wavelength-dependent persistent luminescence from single-component nonstoichiometric $CaGaXO_4$:Bi for dynamic anti-counterfeiting, *Light: Sci. Appl.*, 2024, **13**, 286.

9 Q. Kuang, X. Hou, C. Du, X. Wang and D. Gao, Recent advances in the anti-counterfeiting applications of long persistent phosphors, *Phys. Chem. Chem. Phys.*, 2023, **25**, 17759–17768.

10 R. An, P. Du, Y. Wang, X. Wang, S. Song, J. Feng, H. Sun and H. Zhang, Suprahydrostable ultrasmall hybrid cuprous halide with pseudo-net protector for wireless light-triggered rewritable transient display and dynamically recoverable encryption, *Nano Today*, 2024, **56**, 102294.

11 L. Xu, H. Zheng, T. Pang and J. Mao, Multicolor luminescence of hexagonal $NaYF_4$:Yb^{3+}/Ho^{3+}/Ce^{3+} microcrystals with tunable morphology under 940 nm excitation for temperature-responsive anti-counterfeiting, *J. Rare Earths*, 2022, **40**, 406–414.

12 Z. Li, Y. Yan, T. Wang, S. Wang, L. Guo, W. Feng, L. Zhao, Z. Wang, F. Zhao, J. Chen, Z. Zhang, X. Xu and X. Yu, Multi-color mechano-luminescence of $LaGaO_3$:Sm^{3+},Tb^{3+} via trap sharing for anti-counterfeiting and encryption, *J. Rare Earths*, 2023, **41**, 1869–1875.

13 J. Li, G. Li, X. Lu, S. Wang, M. Leng, S. Yang, J. Guan and Y. Long, Magnetically responsive optical modulation: From anisotropic nanostructures to emerging applications, *Adv. Funct. Mater.*, 2024, **34**, 2308293.

14 R. An, Q. Wang, Y. Liang, P. Du, P. Lei, H. Sun, X. Wang, J. Feng, S. Song and H. Zhang, Reversible structural phase transitions in zero-dimensional Cu(I)-based metal halides for dynamically tunable emissions, *Angew. Chem., Int. Ed.*, 2024, e202413991.

15 W. Ren, G. Lin, C. Clarke, J. Zhou and D. Jin, Optical nanomaterials and enabling technologies for high-security-level anticounterfeiting, *Adv. Mater.*, 2020, **32**, 1901430.
16 G. Liu, X. Wu, F. Xiong, J. Yang, Y. Liu, J. Liu, Z. Li, Z. Qin, S. Deng and B.-R. Yang, Fluorescent, multifunctional anticounterfeiting, fast response electrophoretic display based on TiO_2/$CsPbBr_3$ composite particles, *Light: Sci. Appl.*, 2024, **13**, 198.
17 C. Zhang, Q. Yin, S. Ge, J. Qi, Q. Han, W. Gao, Y. Wang, M. Zhang and J. Dong, Optical anti-counterfeiting and information storage based on rare-earth-doped luminescent materials, *Mater. Res. Bull.*, 2024, **176**, 112801.
18 W. Yao, Q. Tian and W. Wu, Tunable emissions of upconversion fluorescence for security applications, *Adv. Opt. Mater.*, 2019, **7**, 1801171.
19 J. Huang, L. Yan, Z. An, H. Wei, C. Wang, Q. Zhang and B. Zhou, Cross relaxation enables spatiotemporal color-switchable upconversion in a single sandwich nanoparticle for information security, *Adv. Mater.*, 2024, **36**, 2310524.
20 X. Yu, H. Zhang and J. Yu, Luminescence anti-counterfeiting: From elementary to advanced, *Aggregate*, 2021, **2**, 20–34.
21 D. Gao, B. Chen, X. Sha, Y. Zhang, X. Chen, L. Wang, X. Zhang, J. Zhang, Y. Cao, Y. Wang, L. Li, X. Li, S. Xu, H. Yu and L. Cheng, Near infrared emissions from both high efficient quantum cutting (173%) and nearly-pure-color upconversion in $NaY(WO_4)_2$:Er^{3+}/Yb^{3+} with thermal management capability for silicon-based solar cells, *Light: Sci. Appl.*, 2024, **13**, 17.
22 M. Yang, H. Gong, D. Yang, L. Feng, S. Gai, F. Zhang, H. Ding, F. He and P. Yang, Research progress on rare earth up-conversion and near-infrared ii luminescence in biological applications, *Chin. Chem. Lett.*, 2024, **35**, 108468.
23 B. Zheng, J. Fan, B. Chen, X. Qin, J. Wang, F. Wang, R. Deng and X. Liu, Rare-earth doping in nanostructured inorganic materials, *Chem. Rev.*, 2022, **122**, 5519–5603.
24 S. Lamon, H. Yu, Q. Zhang and M. Gu, Lanthanide ion-doped upconversion nanoparticles for low-energy super-resolution applications, *Light: Sci. Appl.*, 2024, **13**, 252.
25 P. Du, Y. Wei, Y. Liang, R. An, S. Liu, P. Lei and H. Zhang, Near-infrared-responsive rare earth nanoparticles for optical imaging and wireless phototherapy, *Adv. Sci.*, 2024, **11**, 2305308.
26 S. Liu, L. Yan, J. Huang, Q. Zhang and B. Zhou, Controlling upconversion in emerging multilayer core–shell nanostructures: From fundamentals to frontier applications, *Chem. Soc. Rev.*, 2022, **51**, 1729–1765.
27 P. Singh, S. Kachhap, P. Singh and S. K. Singh, Lanthanide-based hybrid nanostructures: Classification, synthesis, optical properties, and multifunctional applications, *Coord. Chem. Rev.*, 2022, **472**, 214795.
28 Y. Shang, S. Hao, W. Lv, T. Chen, L. Tian, Z. Lei and C. Yang, Confining excitation energy of Er^{3+}-sensitized upconversion nanoparticles through introducing various energy trapping centers, *J. Mater. Chem. C*, 2018, **6**, 3869–3875.
29 X. Zhou, L. Ning, J. Qiao, Y. Zhao, P. Xiong and Z. Xia, Interplay of defect levels and rare earth emission centers in multimode luminescent phosphors, *Nat. Commun.*, 2022, **13**, 7589.
30 C. Wang, D. Liu, G. Wei, J. Huang, Z. An, X. Xu and B. Zhou, Enabling multimodal luminescence in a single nanoparticle for X-ray imaging encryption and anticounterfeiting, *Nano Lett.*, 2024, **24**, 9691–9699.
31 K. R. Mun, J. Kyhm, J. Y. Lee, S. Shin, Y. Zhu, G. Kang, D. Kim, R. Deng and H. S. Jang, Elemental-migration-assisted full-color-tunable upconversion nanoparticles for video-rate three-dimensional volumetric displays, *Nano Lett.*, 2023, **23**, 3014–3022.
32 J. Huang, Z. An, L. Yan and B. Zhou, Engineering orthogonal upconversion through selective excitation in a single nanoparticle, *Adv. Funct. Mater.*, 2023, **33**, 2212037.
33 J. Huang, L. Yan, S. Liu, N. Song, Q. Zhang and B. Zhou, Dynamic control of orthogonal upconversion in migratory core–shell nanostructure toward information security, *Adv. Funct. Mater.*, 2021, **31**, 2009796.
34 P. Lei, R. An, S. Yao, Q. Wang, L. Dong, X. Xu, K. Du, J. Feng and H. Zhang, Ultrafast synthesis of novel hexagonal phase $NaBiF_4$ upconversion nanoparticles at room temperature, *Adv. Mater.*, 2017, **29**, 1700505.
35 Y. Wu, F. Li, Y. Wu, H. Wang, L. Gu, J. Zhang, Y. Qi, L. Meng, N. Kong, Y. Chai, Q. Hu, Z. Xing, W. Ren, F. Li and X. Zhu, Lanthanide luminescence nanothermometer with working wavelength beyond 1500 nm for cerebrovascular temperature imaging in vivo, *Nat. Commun.*, 2024, **15**, 2341.
36 W. Liu, W. Zhang, G. Li and R. Liu, Dual mode emissions with enhanced green up-conversion luminescence by Gd^{3+} doping and down-conversion from Eu^{3+} in $NaMnF_3$:Yb, Er@$NaGdF_4$:Eu, *Dalton Trans.*, 2021, **50**, 10243–10251.
37 Y. Dwivedi, A. Rai and S. B. Rai, Energy transfer in Er:Eu:Yb co-doped tellurite glasses: Yb as enhancer and quencher, *J. Lumin.*, 2009, **129**, 629–633.
38 L. Wang, X. Xue, H. Chen, D. Zhao and W. Qin, Unusual radiative transitions of Eu^{3+} ions in Yb/Er/Eu tri-doped $NaYF_4$ nanocrystals under infrared excitation, *Chem. Phys. Lett.*, 2010, **485**, 183–186.
39 Z. Wang, X. Li, S. Yin, X. Guo and W. Qin, Phase transition and luminescent properties of the Eu^{3+} ions-doped $NaYF_4$: Yb, Er nanoparticles, *Funct. Mater. Lett.*, 2022, **15**, 2251013.
40 J. Zhou, Y. Teng, X. Liu, S. Ye, X. Xu, Z. Ma and J. Qiu, Intense infrared emission of Er^{3+} in $Ca_8Mg(SiO_4)_4Cl_2$ phosphor from energy transfer of Eu^{2+} by broadband down-conversion, *Opt. Express*, 2010, **18**, 21663–21668.
41 R. An, P. Du, Y. Liang, S. Liu, Y. Wei, P. Lei and H. Zhang, Achieving orthogonal upconversion luminescence of a single lanthanide ion in crystals for optical encryption, *Small Methods*, 2024, 2301577.
42 X. Chen, J. Vanacken, J. Han, Z. Zhong, L. Li, Y. Han, Y. Liu and V. V. Moshchalkov, Intense infrared upconversion luminescence of $NaGdF_4$:Yb/Tm with controlled intensity, *J. Appl. Phys.*, 2017, **121**, 163103.

